Contributions to Geophysics and Geodesy Vol. 53/3, 2023 (167–190)

Detection of karst features and associated geohazard using ground penetrating radar and 2D electrical resistivity imaging; case study from Sannur protectorate, Egypt

Muhammad A. EL HAMEEDY*, Walid M. MABROUK, Said DAHROUG, Ahmed M. METWALLY

Department of Geophysics, Faculty of Science, Cairo University, Egypt

Abstract: The current work explores the suitability and advantages of utilizing ground penetrating radar (GPR), and electrical resistivity imaging (ERI) in the hazard assessment process of Sannur cave associated with water inrush, structural instability, and engineering uncertainty in the site. The huge cave was discovered during mining of alabaster stone in the Egyptian Eastern Desert and considered a karst feature hosted in Eocene limestone with a several types of speleothems. The area is well-known for its high degree of karstification due to a long period of water erosion and the development of fractures network. Detailed geological and geophysical studies, including geological mapping of the area, 3D laser scan, fracture trend analysis, 2D GPR, and 2D ERI has been carried out to study the suitability of the site for safe touristic activities. GPR data delineated numerous probable cavities and fractures (fissures) within limestone formation due to karstification processes below the road heading down to the cave conformable to those analysed fractures exposed at the surface. The integration of GPR and ERI data in the yard outside the cave opening shows good correlation in the determination of lithostratigraphic sequence and dimensions of two electrically conductive clay lenses in addition to inferred fractures striking NW–SE conformable with outcrop studies of fractures in the vicinity of the cave. Recommendations were proposed to be taken into consideration for preparing the site and the results encourage the integrated application of such geophysical techniques for the reconnaissance and further detailed characterization of the karst features within the area.

Key words: GPR, ERI, karst, sinkhole, alabastrine, limestone

1. Introduction

In the late nineties of 20^{th} century and during mining work for extraction of (Egyptian alabaster stone) a huge cave was discovered and is considered the largest subterranean chamber known in Egypt 70 km southeast of

*corresponding author, e-mail: mashraf@sci.cu.edu.eg

doi: 10.31577/congeo.2023.53.3.1

Beni-Suef in the eastern desert (Fig. 1a) at wadi Sannur with speleothems occurrence (stalactite, and stalagmite) as shown in Fig. 1b present in many shapes (*Blue Sky Travel, 2012*). To visualize the cave area (road leading to the cave) 3D laser scans (Fig. 1c) were conducted to better visualize the setting of the cave. The shape of the cave itself is a single crescent about 350 m long and 15 m width at depths ranging from 10 to 15 m (Fig. 1d), and divided into two sections with different characteristics: left-side and right-side galleries.

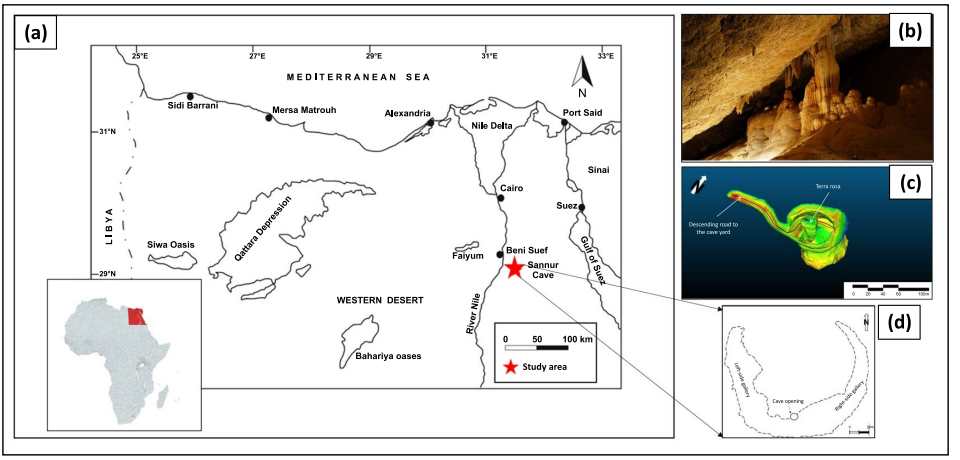

Fig. 1. (a) Location map of the study area; (b) Speleothems (stalactite, and stalagmite) occurrences inside Sannur cave inside left-side gallery. Source: `https://www.flickr.com/photos/blueskytravelegypt/7846339364/`; (c) Three-dimensional laser scans for the road leading to the cave, and terra rosa. Colouring refers to density of coverage points (red = high coverage, and blue = low coverage); and (d) Schematic diagram showing detailed boundaries of the cave illustrating the crescent shape of the cave.

The study area is characterized by high degree of karstification (Fig. 2). Karst is a geological feature resulting in subsurface cavities due to dissolution effect on carbonate rock (*Gilli, 2015*), *Milanović et al. (2019)*, *Redhaounia et al. (2015)*, *Chalikakis et al. (2011)* have focused on the discussion of karst development depending on near-surface geophysical data. With time such chemical erosive process causes the development of cavities which may reach the surface creating sinkholes (*dos-Reis et al., 2014; Gómez-Ortiz and Martín-Crespo, 2012*). Many geological settings are very complex and not cost-effective to evaluate using drilling neither safe (*El Hameedy et al.,*

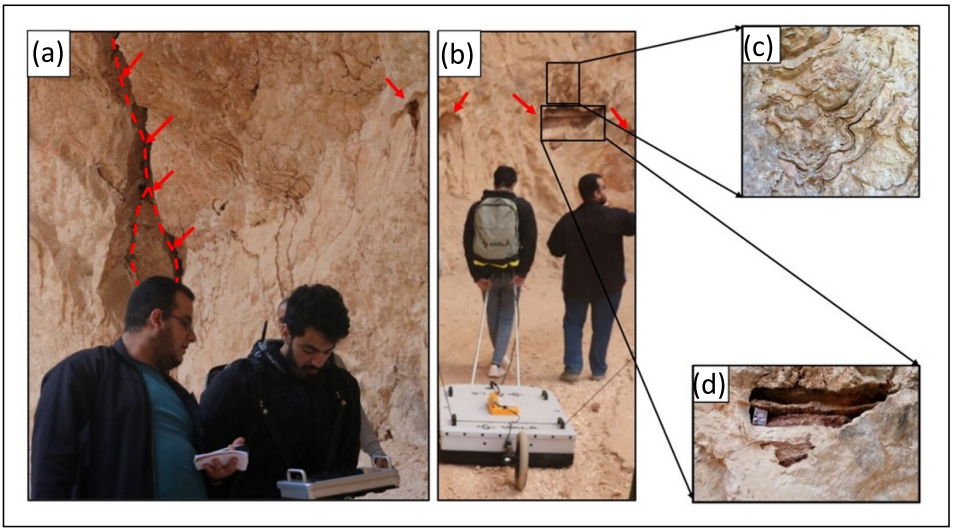

Fig. 2. Recrystalized limestone to Egyptian alabaster associated with high degree ok karstification along descending road to cave yard. (a) large fracture along the wall of the road descending to the cave yard working as water conduit; (b) karst features along the way to the road; (c) zoomed photograph of hummocky-shaped Egyptian alabaster; (d) relatively large karst within Eocene limestone unit.

2023a; Slob et al., 2010). However, geophysical techniques are suitable for such case because they are cost-effective rapid and non-invasive techniques.

Ground penetrating radar (GPR) and Electrical resistivity imaging (ERI) are a widely used geophysical techniques used in resolving environmental and engineering problems (i.e., *El Hameedy et al. 2023b; Ganiyu et al., 2020; Aziz et al., 2019; Xie et al., 2018; Auken et al., 2014a,b*). Many studies related to karst environments and sinkholes using GPR data integrated with ERI technique in different geological structural settings (i.e., *de Oliveira et al., 2020; Ali et al., 2020; Abidi et al., 2018; Gómez-Ortiz and Martín-Crespo, 2012; Pueyo-Anchuela et al., 2010; Kruse et al., 2006; El-Qady et al., 2005; Zhou et al., 2002*).

The objective of the work is to map the voids related to karstification processes in the vicinity of the cave. GPR technique itself is capable to detect such karst features, due to its high-quality images of subsurface. However, obtaining such high-quality data in fractured and karstified carbonate environments is not a simple process (*Grasmueck et al., 2013*) because the filling

material in the voids could be electrically conductive. Hence, as a result, the signal will attenuate much greater, limiting the depth of penetration and image resolution (*Xavier Neto and de Mederios, 2006; Bano, 1996a,b*). On the other hand, the importance of ERI appears during studying heterogeneity of the subsurface, especially in a karst environment with voids filled with clays and conductive weathered materials, which is the case at Sannur cave.

Furthermore, since 1992 one of the major questions is: What happens to the large quantity of water infill due to 1990's floods which filled the whole cave? Where did the water infiltrate? Figure 3e shows a recent collapse at the left-side gallery of the cave, and two major sinkholes were noticed along with extensive mud cracks at the floor of the right-side gallery of the cave (Fig. 3f). Similarly, *Günay et al. (1997)* proposed a scenario for the case of water infiltration that assumes an additional cave below the current one that retains the infiltrated water through a system of fractures beneath the cave floor, which is also supported by some of the evidence from the results of this research.

Centre of environmental hazard mitigation at Cairo University (CEHM) prepared an expedition to Sannur cave in 2002 to study the geological framework of the cave and predicted that "there might be another cave below the current cave at depth not less than 20 m". The maximum depth they reached were 18 m using vertical electrical sounding (VES) technique due to the inner dimensions of the cave which limits the length of the profile and as a result limiting the depth of penetration. In this study 2D GPR as shown in Fig. 3a and 2D ERI (Fig. 3b) data were utilized to delineate the voids and sinkholes outside, and inside the cave.

During geological outcrop measurements within the hill above the cave, a small hole in the ground were discovered as shown in Fig. 3g, and two perpendicular radar sections were acquired just above this opened hole to delineate the extension of such hole.

The lack of geophysical studies in Sannur cave and its vicinity, despite of few geological studies about geomorphology of the geological features (*Günay et al., 1997*), radioactive age dating and natural radioactivity of the cavern (*Amin and Eissa, 2008; Amin et al., 2008; Dabous and Osmond, 2000*), motived the authors to conduct the current geophysical work so it could help in the safety of the site to make it possible for people to visit this

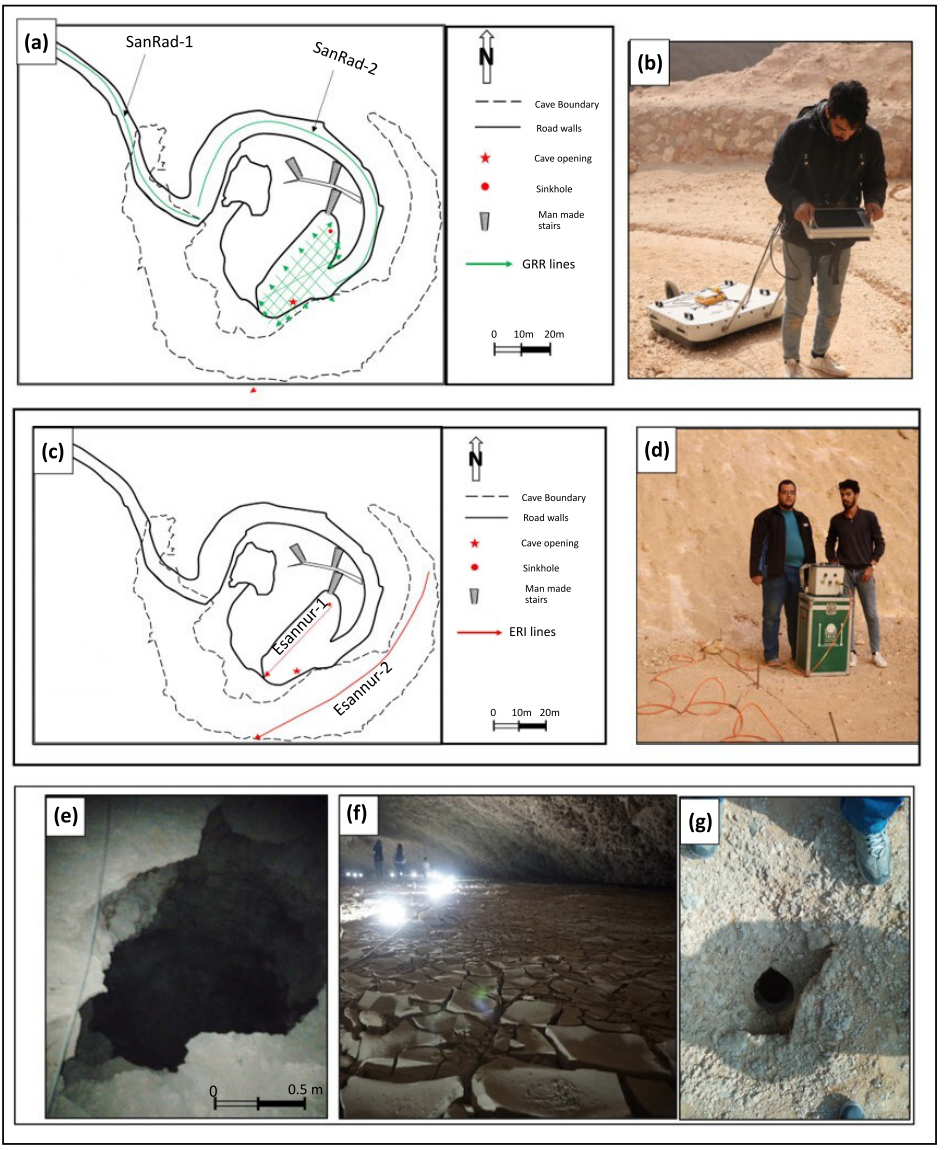

Fig. 3. (a) Layout of (GPR) survey lines; (b) 100 MHz antenna during data acquisition along road to the cave; (c) Layout of (ERI) survey lines; (d) during data acquisition in front of cave opening within the cave yard; (e) Recent collapse in the left-side gallery; (f) extensive mud cracks on the cave floor in the right-side gallery of Sannur cave; (g) open-hole discovered within the hill directly above the cave.

spectacular cave. It is important element of geological heritage and geotourism activities (*Stepišnik and Trenchovska, 2018; Gilli, 2015*), and such heritage have been discovered in few different localities in Egypt (*Tomassetti et al., 2016; Wanas et al., 2009; El-Qady et al., 2005; Vermeersch et al., 2005; Brook et al., 2002*) not just at Sannur area. However, these studies are still insufficient to understand the geological heritage of these caves and to make the best use of them.

2. Description and geology of the study area

The study area is located east of the Nile River, approximately 200 km from Cairo and 70 km from Beni-Suef Governate centre. Three geomorphological features in the study area could be distinguished in Fig. 4a, including dissected plateau, pediments, and playa (*Hassan et al., 1978*). The highest altitude (approximately 335 m) is at Gebel Homret Shaiboun. The plateau consists of limestone and marl beds dissected by several wadis-oriented E–W draining the plateau towards the Nile River.

Sedimentary succession cropping study area ranges in age from middle Eocene to Pliocene Fig. 4b. Mokattam Formation (Mokattam Fm) composed mainly of limestone rich in foraminifera with thin intercalations of shale and clays. The depositional environment of Mokattam Fm is shallow marine platform (*Sallam et al., 2018a*). Qurn Fm consists of limestone, marl, and shale with a shallow marine to very shallow marine (shelf lagoon reef) depositional environment (*Sallam et al., 2015*).

Wadi Hof Fm composed of greyish limestone, sandy limestone, and shale intercalations (*Sallam et al., 2020*) which deposited on a restricted platform and tidal flats (*Farag and Ismail, 1959*). Umm Raqaba Fm consists of intercalations of fossiliferous conglomerates and sand beds with a shallow marine depositional environment (*Issawi et al., 2005*) and represents a middle Pliocene regressive phase (*Sallam et al., 2018b*).

Numerous NW–SE trending normal faults were mapped in the area as shown in Fig. 4c. The area is generally flat with very gentle slopes (1° to 2°) in various directions. Several smaller faults have been mapped, such as the Gebel Tarboul Fault, the Gebel Homret Shaiboun Fault, the Gebel Umm Ragaba Fault, and the Wadi Sannur Fault (*Hassan et al., 1978*).

The presence of these faults developed a fracture system and joints as

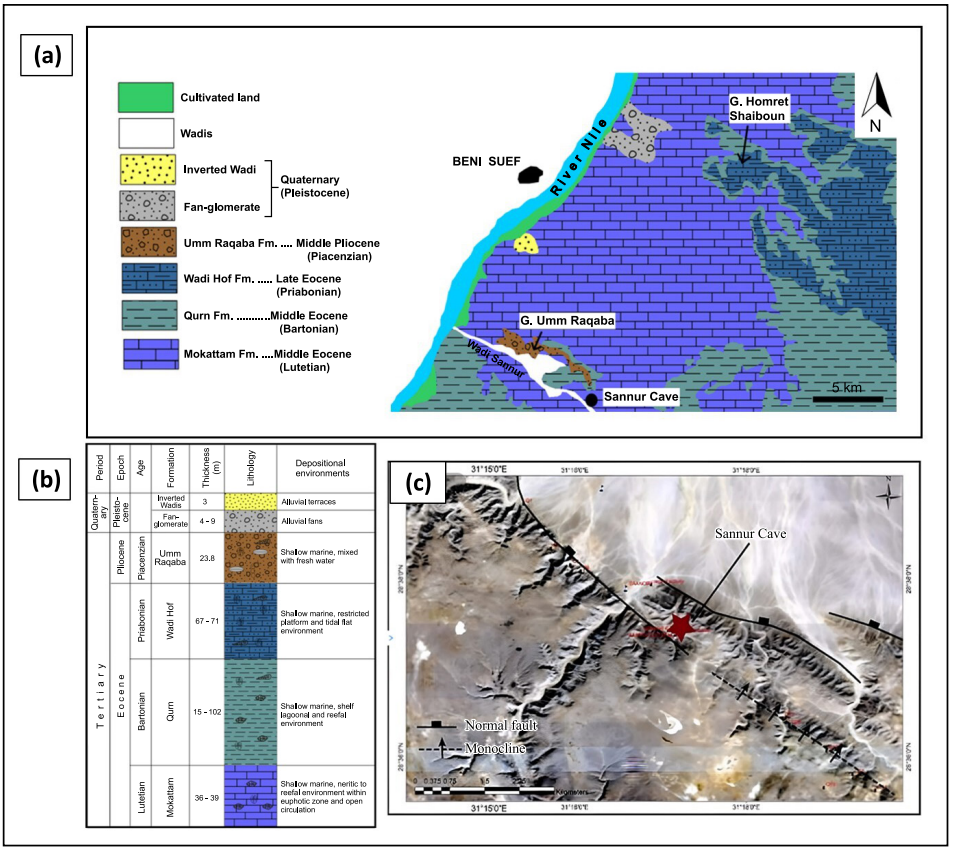

Fig. 4. (a) Geology of the study area after (*Sallam et al., 2020*); (b) Stratigraphic column of the study area modified after (*Sallam et al., 2020*); (c) Landsat satellite image showing Sannur cave position on the upthrow of normal fault striking NW–SE.

delineated in Fig. 5 as a result, facilitated the karst processes, and these fracture systems worked as a passage and conduit of conduit of water solution that dissolved middle Eocene Mokattam limestone and recrystallize it as speleothems in several shapes and sizes through time. That is, studying those fractures as shown in Fig. 5b and Fig. 5e (frequency, trends, and its displacements/opening along those fractures) plays a vital rule in geohazard assessment processes of the study area. Therefore, two rose diagrams were prepared for joints and fractures of the two walls where the cave are hosted within. The first rose diagram in Fig. 5c for the wall adjacent to

the cave opening shows a major trend in NW–SE direction, and NNE–SSW dominant trend for the wall descending to the cave (Fig. 5f).

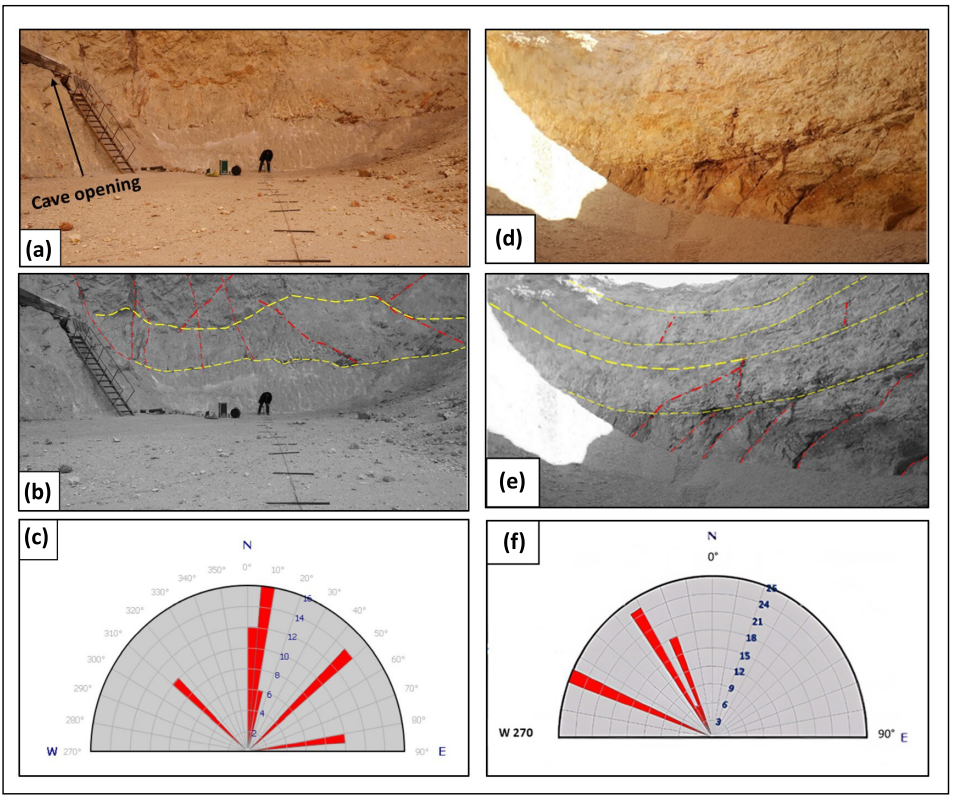

Fig. 5. (a) photo of the wall adjacent to the cave; (b) bedding planes (yellow lines) and fractures (red lines) within the limestone; (c) fracture analysis (frequency and trends) of the dominant fractures within this wall (d) Photo of the wall of the road leading to the cave; (e) bedding planes and fractures; (f) fracture analysis within this wall.

3. Materials and methods

In the current study two geophysical techniques were applied, Electrical Resistivity Imaging (ERI), and Ground Penetrating Radar (GPR). This section provides a background on these techniques along with acquisition parameters and processing steps adopted for the data acquired.

3.1. Electrical Resistivity Imaging (ERI)

Direct Current (DC) resistivity is a popular and well-established geophysical method (*Telford et al., 1990*). It employs two electrodes (namely current electrodes) to inject current into the subsurface, another two electrodes called potential electrodes are used to measure the potential difference at a point just in the middle between current electrodes. These observed potential differences are converted to apparent resistivity pseudo-sections that reflect the electrical resistivity structure of subsurface materials, which in turn depends on many factors (temperature, porosity and permeability, fluid saturation and salinity, and mineralogy (*Spichak, 2020*)).

As we previously mentioned in section 1, (ERI) has been employed effectively in karst investigations as their structures, soil cover and void shape and, more significantly, the characterization of cavity sediments, the study of which is critical for the related geological risks (*Ganiyu et al., 2020; Xie et al., 2018*). Therefore, the approach may be utilized as a control for the result accuracy evaluation of the other applicable geophysical method employed (GPR). Hence, to identify and map karst features in the region, we conduct two geo-electrical survey lines (Fig. 3c). The base electrode spacing was 1.5 m in the cave yard (Esannur-1), and 5 m within the right-side gallery of the cave (Esannur-2). 24 electrodes were utilized to deliver electrical current utilizing dipole–dipole array geometry. Such array was tested by (*Putiška et al., 2012*) emphasising its advantage for cavities detection and imaging. Then, the resistivity datasets were gathered by installing the Syscal-Pro system with a multi-electrode cable that is a high-resolution system for DC resistivity measurements in Fig. 3d.

Processing of resistivity data is done by importing field data to Prosys II software to detect anomalies and errors in the data. The apparent resistivity values that were extremely high were deleted manually from the dataset. After that, ResIPy python package (*Blanchy et al., 2020*) was applied to invert the data to acquire the true resistivity model of the subsurface. Inversion is to recreate the geological model that obtained by synthetic data matching with observed data. But due to inconsistencies and noise interference within observable data, the model rebuilding is ill-posed (many solutions could fit the observed data). Accordingly, tomographic inversion is usually described as an optimization of data fitting with regularization of the model. Tomographic inversion is often accomplished using a normal

conjugate gradient approach, which needs the gradient and Hessian matrix of an objective function to be computed. And there are two kinds of objective functions that can be used. The first is the L_1-norm, while the second is the L_2-norm (*Zhou, 2018*).

3.2. Ground Penetrating Radar (GPR)

Ground Penetrating Radar (GPR) is a non-invasive geophysical technique that images the subsurface in the form of cross-sections (radargrams) resembling reflection profiles in appearance (*Reynolds, 2011*). The propagation, reflection, and scattering of electromagnetic pulse – usually ranging from 10 to 2000 MHz – beneath the ground is the basis for GPR data acquisition. The transmitter antenna sends the electromagnetic pulse to the subsurface. The retrieved signals (amplitude and travel times) are recorded by a receiver antenna with an excellent resolution compared to the other near-surface geophysical techniques (electrical resistivity).

Depth of penetration and resolution is a function in antenna frequency, clay, and water content. Hence, to reach greater depth, a lower frequency antenna must be chosen at the expense of resolution acquired, and the size of the feature must be relatively large to be detected at greater depths. The amplitude of radar pulse is critical as it may convey information about the subsurface. After time to depth conversion of radar data, these amplitudes aid in mapping subsurface discontinuities (*de Olivera et al., 2020*). Such amplitudes are more prominent when the contrast at the boundary of these discontinuities is higher and vice versa.

For our study, the GPR survey was conducted using MALA ProEx GPR (MALÅ Geoscience) system with a 100 MHz shielded antenna in Fig. 3b. The data acquisition process was divided into three stages; the first one was 2-D, and two Radargrams (SanRad-1 and SanRad-2), with a length of 96 m and 146 m, respectively were acquired in order to map any voids or fracturing present below the road leading down to the cave entrance. It is noteworthy that this road was made initially for a mining quarry in the area before the discovery of the cave, and it cuts through middle Eocene limestone (Mokattam Fm). The second stage was a 2D Grid survey in the yard in front of the cave opening (Fig. 3a) to map subsurface fractures and voids and study the subsurface's lithostratigraphic sequence—the final stage was 2D radargrams at the hill directly above the cave to study an opened hole in

the ground which interpreted later as a relatively small subterranean cavern (Fig. 3g).

ReflexW (Sandmeier Inc., ver. 8.1, 2016, Germany – *Sandmeier, 2016*) was utilized to process the data. The basic goal of all the processing processes is to find and eliminate undesired effects or artefacts in the GPR data. Following steps indicate the main processing workflow adopted to process raw GPR data: removing direct waves to obtain a zero-offset section, 1D low frequency noise removal filter (dewow), combined linear and exponential gain, 2D background noise removal filter, bandpass Butterworth filter, spectral balancing. Such processing steps were adopted after (*de Oliveira et al., 2020*) that focuses on GPR data processing in carbonate karst environment.

4. Results and discussion

In this section we will view the results obtained from two geophysical techniques used and interpret these results from a geological point of view.

4.1. Electrical Resistivity Imaging (ERI)

Results of the two resistivity profiles SanRes-1 taken at the cave yard in front of cave opening outside the cave, and SanRes-2 taken inside the right-side gallery of the cave are shown in Fig. 6.

Inversion results of profile SanRes-1 shown in Fig. 6a prove that there are two distinctive lithostratigraphic units as is shown here: lens-shaped conductive weathered carbonates and sediments with considerable amount of moisture, and highly resistive bulk alabastrine limestone. Anomalies R1, and R2 interpreted on profile SanRes-1 could be attributed to local depressions filled with conductive weathered materials which is transported by seasonal rain fall, but anomaly R3 we interpret as it is formed by karstification and infiltration of water, which enhance the dissolution process of carbonate rocks which leads to epikarst feature (collapse) that is considered a geological hazard and should be taken into consideration.

In Fig. 6b inversion results of profile SanRes-2 indicate the presence of similar lithostratigraphic units as the one of profile SanRes-1. The first unit is a several lens-shaped conductive weathered materials (carbonates and sediments with moisture content) with an average thickness of 6 m,

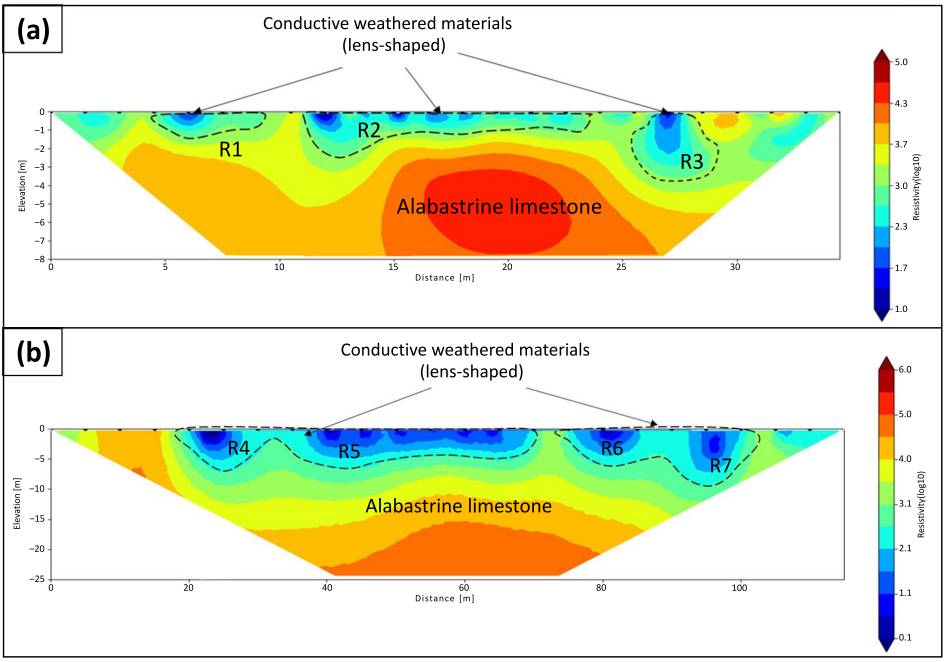

Fig. 6. Electrical resistivity imaging (ERI) inversion results of profiles: (a) SanRes-1 at the cave yard in front of the cave opening highlighting three anomalies. R1, R2 interpreted as local depressions filled with weathered conductive materials, while anomaly R3 is considered epikarst feature (doline) due to water infiltration which enhanced the karstification process and finally lead to a collapse and considered a geohazard in our case to be taken into consideration; (b) Electrical resistivity imaging (ERI) inversion results of profile SanRes-2 in the right-side gallery of the cave. Anomalies R4, R5, R6, and R7 are attributed to dissolution processes of limestone which is supposed to be water carriers to deeper cavern.

and highly resistive alabastrine limestone to the bottom of the section. It should be mentioned that in the early nineties the cave was fully submerged under water because of floodings that took place in Wadi-Sannur, so the responsible authorities constructed a flood protection system around the cave to prevent the water from reaching the cave.

Anomalies R4 to R7 could be attributed to dissolution processes of limestone and as we mentioned above considered a geological hazard because of the water content of this lenses may cause further dissolution of surrounding limestone and formation of new sinkhole (collapse) of cave floor as shown in

Fig. 3e, which represents a recent collapse in the cave floor near the left side gallery 1.8 m wide and approximately 3.5 m deep. Future collapse like this one exposes the people visiting the cave to great danger so the conductive weathered material (i.e., anomalies R4, and R7) in the cave needs to be further studied to ensure the safety of the cave floor.

4.2. Ground Penetrating Radar (GPR)

Results in Fig. 7, and Fig. 8 represent the first acquisition phase of GPR survey along the road down leading to the cave as shown in Fig. 3a (green lines) to study the lithology of subsurface layers and delineate karst features and caves if any. Radargram SanRad-1 shows several distinctive features. The most distinctive one is relatively large two cavities at depth 9 m at distance 57 m to 68 m marked with red hyperbolas illustrating top of left-side gallery of Sannur cave, also the bottom of the left-side gallery was distinguished, and the height of the cave calculated from radar results correlates with the actual height of the cave which is 9 m. The second one is relatively high amplitude features embedded within alabastrine limestone, which indicated karst features in red rectangular as the one shown in Fig. 7b. Such karstified area extends to the wall in Fig. 10b.

Radargram SanRad-2 results shown in Fig. 8 shows similar features of large cavities at distance 30 m, 55 to 70 m, and 108 to 120 m at depths ranging from 5 m to 21 m, also a high degree of karstification in shown in this profile as marked in red rectangles of relatively high amplitudes. The lithology of subsurface layers can be classified into three units depending on GPR response the first unit is marked in yellow fill and represents recent fill of limestone and alabaster to flatten the road after mining work done there and ranging in thickness from 0.5 m to 5.5 m. While the second lithological unit is intact limestone with almost no karst, and finally, the last unit is karstified limestone of relatively high contrast in amplitudes.

Second phase shown in Fig. 9 and Fig. 10 represents results in the cave yard that clarified many karst features and cavities with different dimensions as highlighted with red hyperbolas representing cavities and red rectangulars as a karstification zones. Some of them poses a threat on the integrity of subsurface at cave yard. Similar lithological units to those in the SanRad-1 and SanRad-2 profiles, with a modern infill material of carbonate fragments, alabaster, and sandstone extend to a depth of 2 m. Another unit is the

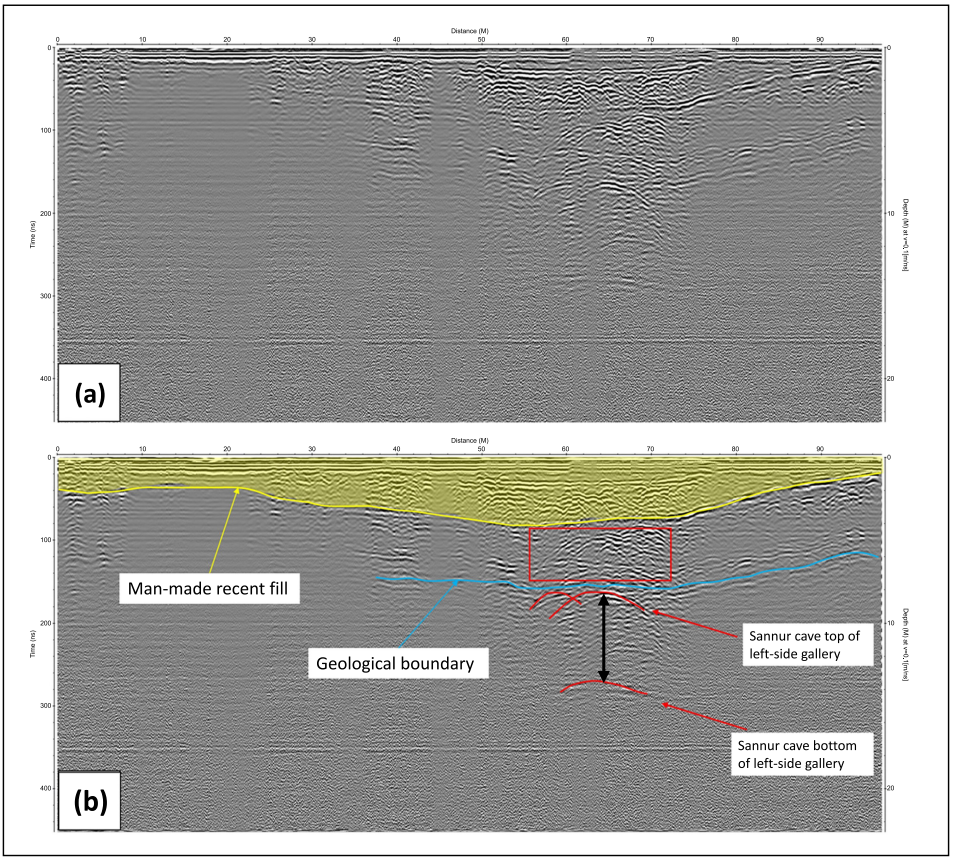

Fig. 7. Processed GPR of profile SanRad-1 (a) before interpretation, and (b) after interpretation. Red rectangle showing area of extensive karstification. Height of the left-side gallery were delineated from the dataset as indicated by black arrow with a calculated height of 9 m which is the true height of the cave.

karstified limestone with fractures filled with sediments with a significant amount of moisture, giving a relatively high contrast amplitude, and the final unit is alabastrine limestone lack in karstification and voids.

Finally, the third phase results (Fig. 11) represent the data acquired on the hill directly above the cave. Two perpendicular radargrams were acquired traversing the exposed small hole (Fig. 3g), and studying such anomaly gives us the opportunity to understand the water infiltration processes and pathways that may led to formation of the Sannur cave.

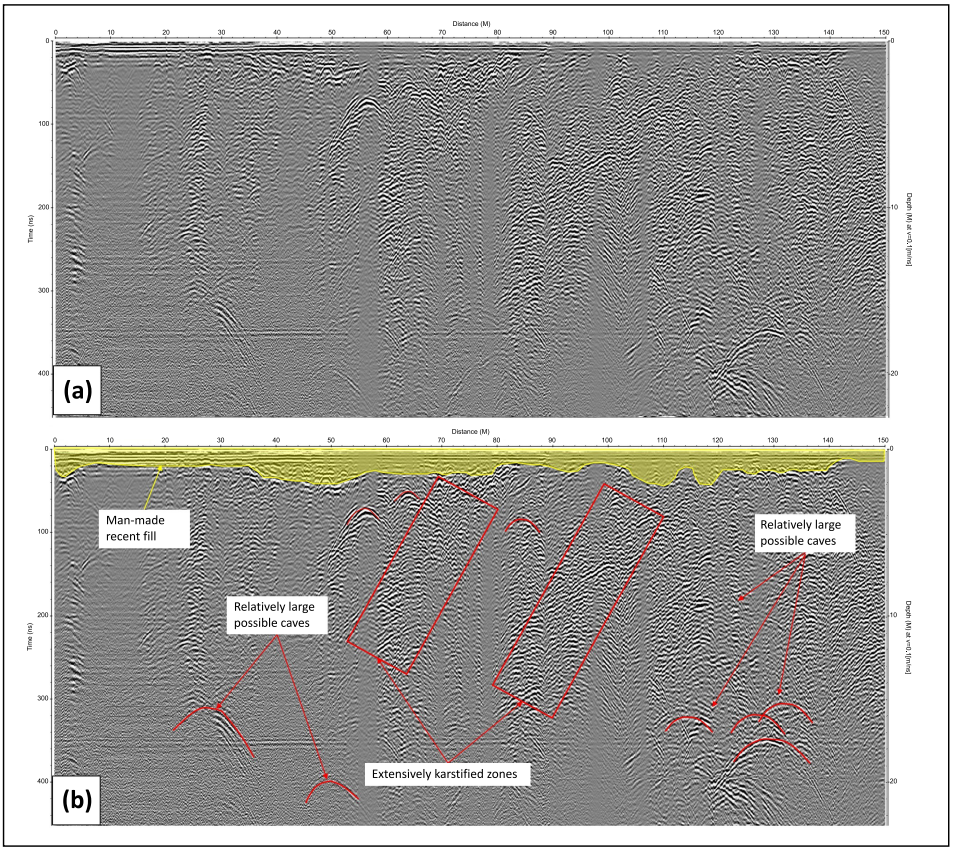

Fig. 8. Processed GPR of profile SanRad-2 (a) before interpretation (b) after interpretation. Red rectangle showing area of extensive karstification, and red hyperbolic shapes representing probable locations of subsurface cavities.

In addition to producing easily visible anomalies, the air-filled cavities formed an asymmetrical pattern of high amplitudes that is indicative of fractures associated with the karstification and recrystallization of Mokattam Fm due to large resistivity contrast between air filling the cave and surrounding limestone. According to the geophysical characterization of resistivity cross sections, almost all parts of the ERI tomographs are dominated by high-resistivity values reflectng intact limestone free of infiltrated water and weathered conductive materials. In addition, a group of low-resistance zones was detected, and these were identified as pockets of conductive weath-

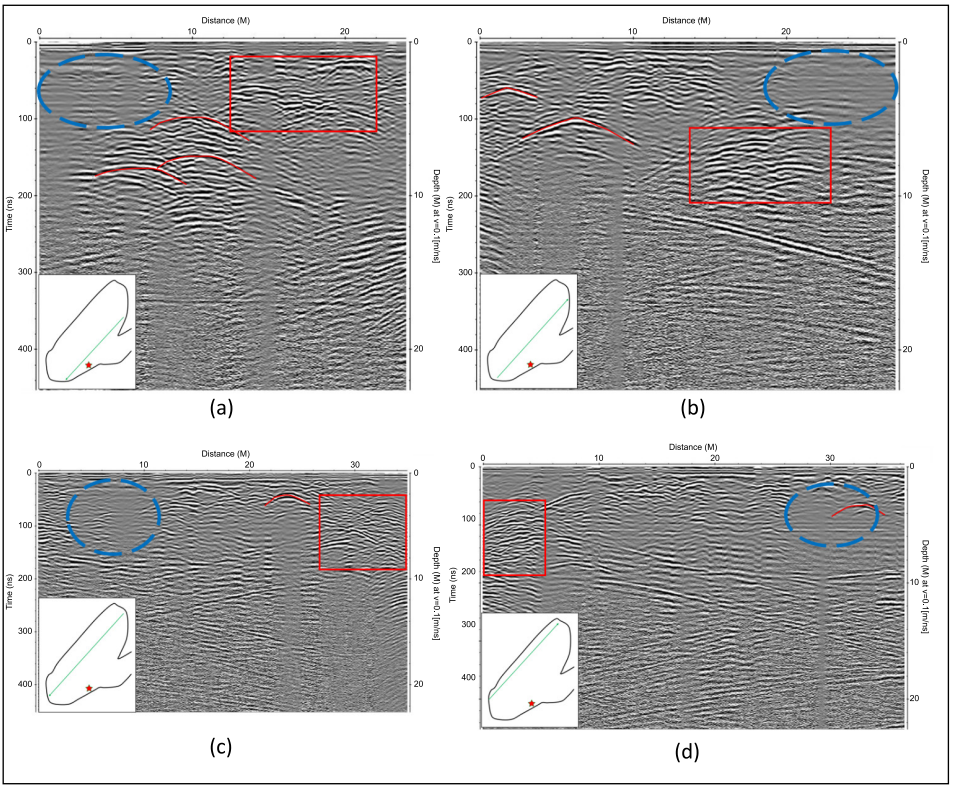

Fig. 9. Processed and interpreted GPR of longitudinal profiles at the cave yard with the red hyperbolas indicating positions of possible subsurface caverns, red rectangular indicating high karstification zones, and blue circles indicating high attenuation of radar signals due to presence of sinkhole used to collect excess rainfall seasonal water. Bottom left of each radargram indicates the relative position of the radargram in the cave yard.

ered materials. These lenses depict an epikarst feature (dolines) that was collapsed and was discovered in the left side gallery (Fig. 3e).

The hyperbolic radar signal from a cave at a depth ranging from 5 m to more than 17 m, with a width of 1 up to more than 8 m, is revealed by the processed GPR data along the road leading down to the cave. This finding is in good accordance with the known cave system in the study area. Additionally, a few anomalous zones have been identified and are thought to represent minor karstic structures and possible branches of the cavern system.

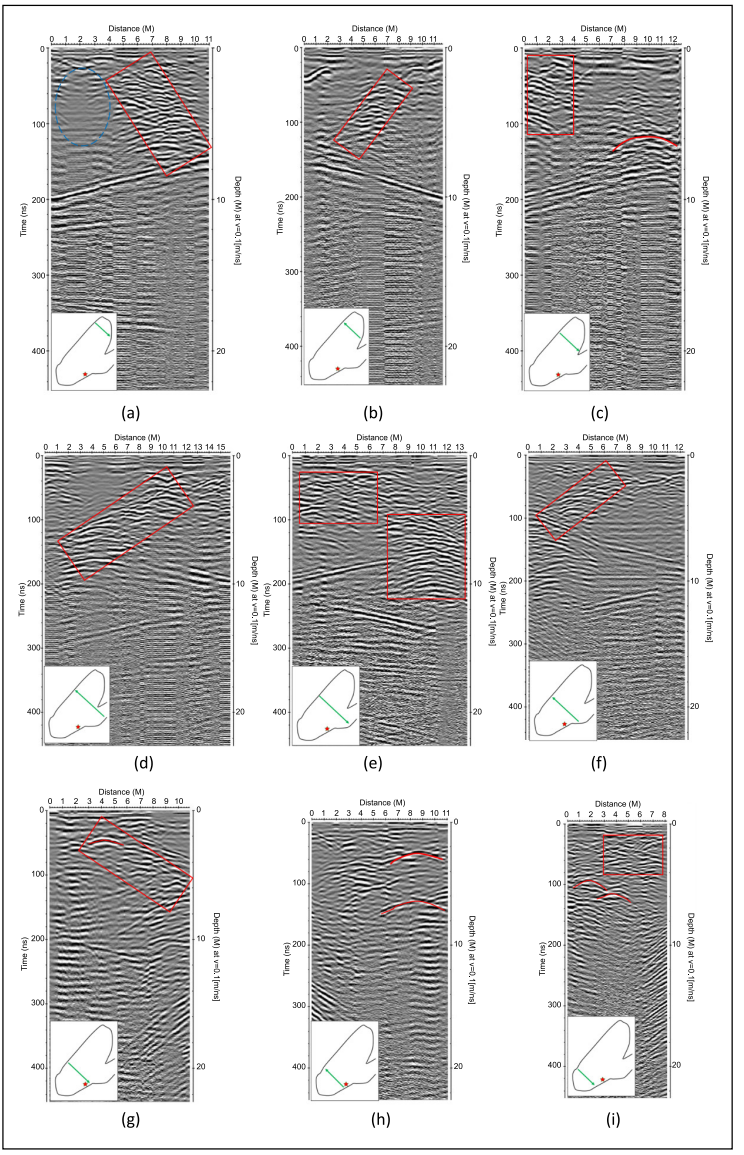

Fig. 10. Processed and interpreted GPR of traverse profiles at the cave yard with the red hyperbolas indicating positions of possible subsurface caverns, red rectangular indicating high karstification zones, and blue circles indicating high attenuation of radar signals due to presence of sinkhole used to collect excess rainfall seasonal water. Bottom left of each radargram indicates the relative position of the radargram in the cave yard.

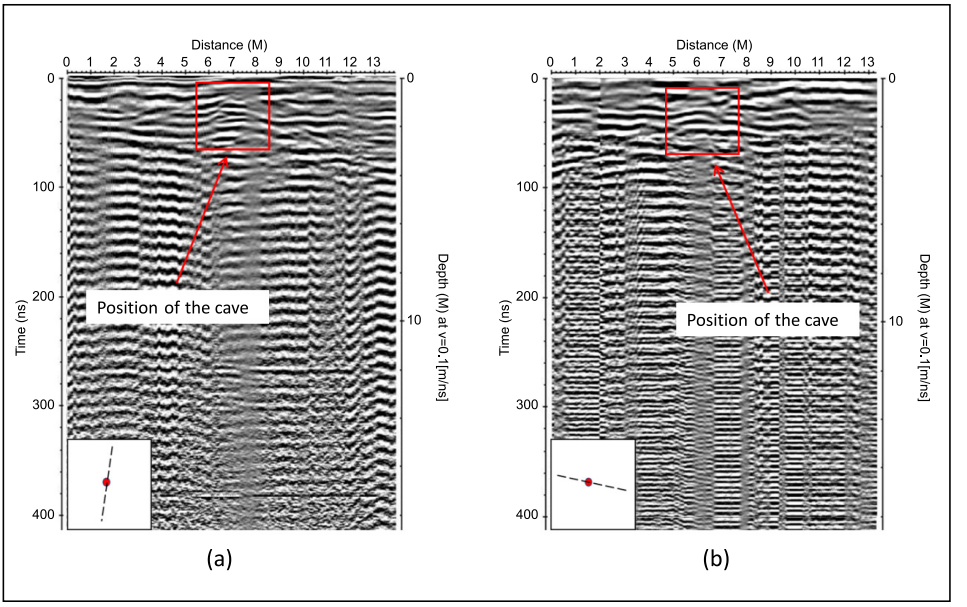

Fig. 11. Processed and interpreted GPR of (a) longitudinal profile and, (b) Traverse profile over the opened hole with the red rectangular indicating positions and extension of that caverns. The bottom left corner of each radargram indicates the relative position of the radargram relative to the hole opening.

Good correlation between electrical resistivity data and radar data at the cave yard were clearly and concisely noticed as the anomaly of the sinkhole area in the subsurface which were used to collect excess of seasonal rainfall water can be delineated from electrical resistivity data as a low resistivity anomaly (R3 in Fig. 6a), also visible clearly and correlates with radar data as a great attenuation of radar signals as shown in Figs. 9b, 9c, and 9d as a blue circle, which took place at the zone of the sinkhole. As well, the karstification zones direction determined from radar data are conformable with those studied from outcrops of the walls surrounding the cave (Fig. 5).

Figure 12 represents a conceptual model for the situation of Sannur cave showing two galleries with speleothems occurrences visualizing the proposed hypothesis of existence another cave below the main one at depth not less than 20 m.

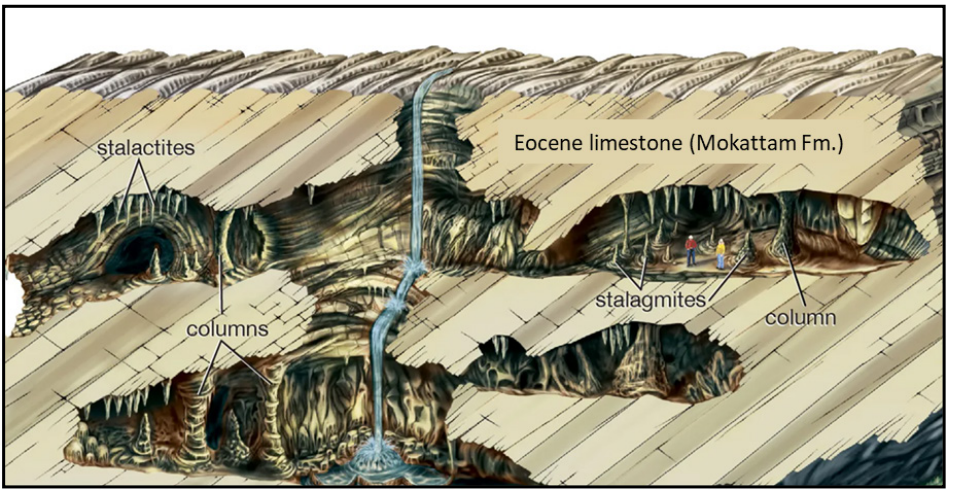

Fig. 12. Image conceptualizing the situation of Sannur cave showing two galleries with speleothems occurrences and visualizing the proposed hypothesis of existence another cave below the main one at depth not less than of 20 m. Source: cross-section of a cave. Image. Encyclopædia Britannica, (*Encyclopædia Britannica*). `https://www.britannica.com/science/karst-geology#/media/1/312718/112257`. Accessed 10 Nov. 2022.

5. Conclusion

Sannur cave is one of the significant, non-renewable, and geologically important resource for studying rare speleothems occurrences in many diverse shapes and sizes. A collapse inside the cave took place recently so that it was important to study the area for subsurface cavities so that the site could be prepared for geo-tourism activities. Two geophysical techniques were conducted in the area, GPR and ERI for this purpose.

The objective of this study was to investigate the stability of road descending to the cave, cave yard fracture system, and shallow subsurface setting of the cave to outline its geologic structures and associated hazards. Two-dimensional resistivity imaging using dipole-dipole array and ground penetrating radar data were collected and interpreted.

We can infer from the findings of this study that electrical resistivity and ground-penetrating radar have shown to be effective techniques for imaging subsurface caverns in limestone at shallow depths. Combining the two geophysical approaches has proven to be effective in mapping low resistivity

zones (electrically conductive material) that emerged as an epikarst feature (depressions) filled with weathered materials and clays. Furthermore, numerous large cavities were found from GPR images below the road descending to the cave, and at the cave yard varied in size and depth. Several possible karst features, i.e., fissures and water conduits, were interpreted on the GPR images.

Finally, the identified fracture zones and karstic features can be regarded as the primary source of potential future cracking at this site due to the regular seasonal rainfall in the study area. As a result, we advise creating a rainwater drainage system around the cave and accelerating the treatment of the significant voids and karstic features that have been identified along the road leading to the cave and within the cave yard.

This is a preliminary study, part of broader future research in the region, which has the possibility to use this effective approach for the full area. It is strongly advised in the following steps to enlarge the cave entrance, and develop adequate lifting instruments, so that the GPR antenna can be brought securely to the cave.

Acknowledgements. Author would like to acknowledge the Centre of environmental hazard mitigation at Cairo university (CEHM) for their support and for providing the access to the cave. Ministry of Environment (Egyptian Environmental Affairs Agency) for facilitating the conditions for a safe data acquisition.

Data and materials are readily available. Datasets created or analysed in the development of the current study are available from the corresponding author upon reasonable request.

Code availability. There is no code available in this work.

Authors' contributions. All authors contributed to the study conception and design. Material preparation, data collection and analysis were performed by the following authors: [Muhammad Ashraf El Hameedy], [Waleed Mohamed Mabrouk], [Ahmed Mohsen Metwally], and [Said Dahroug]. Data acquisition for both ERI and GPR field dataset by [Ahmed M. Metwally], and [Muhammad A. El Hameedy]. The first draft of the manuscript was written by [Muhammad Ashraf El Hameedy] and all authors commented on previous versions of the manuscript. All authors read and approved the final manuscript.

Declarations. All authors certify that they have no affiliations with or involvement in any organization or entity with any financial interest or non-financial interest in the subject matter or materials discussed in this manuscript.

References

Abidi A., Demehati A., Banouni H., El Qandil M., 2018: The Importance of Underground Cavities Detection in the Choice of Constructible Areas: Case of the Agglomeration of Fez (Morocco). Geotech. Geol. Eng., **36**, 3, 1919–1932, doi: 10.1007/s10706-017-0425-3.

Ali M. A. H., Sun S., Qian W., Dodo B. A., 2020: Electrical resistivity imaging for detection of hydrogeological active zones in karst areas to identify the site of mining waste disposal. Environ. Sci. Pollut. Res., **27**, 18, 22486–22498, doi: 10.1007/s11356-020-08738-9.

Amin R. M., Eissa M. F., 2008: Radon level and radon effective dose rate determination using SSNTDs In Sannur cave, Eastern desert of Egypt. Environ. Monit. Assess., **143**, 1-3, 59–65, doi: 10.1007/s10661-007-9957-y.

Amin R. M., Mansy M., Eissa M. F., Eissa H. M., Shahin F. M., 2008: Assessment of natural radioactivity and radon exhalation rate in Sannur cave, eastern desert of Egypt. J. Radiol. Prot., **28**, 2, 213–222, doi: 10.1088/0952-4746/28/2/005.

Auken E., Christiansen A. V., Kirkegaard C., Fiandaca G., Schamper C., Behroozmand A. A., Binley A., Nielsen E., Effersø F., Christensen N. B., Sørensen K., Foged N., Vignoli G., 2014a: An overview of a highly versatile forward and stable inverse algorithm for airborne, ground-based and borehole electromagnetic and electric data. Explor. Geophys., **46**, 3, 223–235, doi: 10.1071/EG13097.

Auken E., Doetsch J., Fiandaca G., Christiansen A. V., Gazoty A., Cahill A. G., Jakobsen R., 2014b: Imaging subsurface migration of dissolved CO_2 in a shallow aquifer using 3-D time-lapse electrical resistivity tomography. J. Appl. Geophys., **101**, 31–41, doi: 10.1016/j.jappgeo.2013.11.011.

Aziz N. A., Abdulrazzaq Z. T., Agbasi O. E., 2019: Mapping of subsurface contamination zone using 3D electrical resistivity imaging in Hilla city, Iraq. Environ. Earth Sci., **78**, 16, 502, doi: 10.1007/s12665-019-8520-9.

Bano M., 1996a: Constant dielectric losses of ground-penetrating radar waves. Geophys. J. Int., **124**, 1, 279–288, doi: 10.1111/j.1365-246X.1996.tb06370.x.

Bano M., 1996b: Modeling and inverse Q imaging of ground penetrating radar waves in 1 and 2D. Geophys. Res. Lett., **23**, 22, 3123–3126, doi: 10.1029/96GL03010.

Blanchy G., Saneiyan S., Boyd J., McLachlan P., Binley A., 2020: ResIPy, an intuitive open-source software for complex geoelectrical inversion/modeling. Comput. Geosci., **137**, 104423, doi: 10.1016/j.cageo.2020.104423.

Blue Sky Travel, 2012: The Sannur Cave Protectorate, Bani Sueif. Flicker, retrieved December 9, 2022, from https://www.flickr.com/photos/blueskytravelegypt/7846339364/.

Brook G. A., Embabi N. S., Ashour M. M., Edwards R. L., Cheng H., Cowart J. B., Dabous A. A., 2002: Djara Cave in the Western Desert of Egypt: morphology and evidence of Quaternary climatic change. Cave Karst Sci., **29**, 2, 57–66.

Chalikakis K., Plagnes V., Guerin R., Valois R., Bosch F. P., 2011: Contribution of geophysical methods to karst-system exploration: an overview. Hydrogeol. J., **19**, 6, 1169–1180, doi: 10.1007/s10040-011-0746-x.

Dabous A. A., Osmond J. K., 2000: U/Th isotopic study of speleothems from the Wadi Sannur Cavern, Eastern Desert of Egypt. Carbonates Evaporites, **15**, 1, 1–6, doi: 10.1007/BF03175643.

de Oliveira J. G. Jr., de Medeiros W. E., de Santana F. L., Bezerra F. H. R., Cazarin C. L., 2020: Enhancing stratigraphic, structural and dissolution features in GPR images of carbonate karst through data processing. Near Surf. Geophys., **18**, 2, 135–148, doi: 10.1002/nsg.12074.

dos Reis J. A. Jr., de Castro D. L., de Jesus T. E. S., Filho F. P. L., 2014: Characterization of collapsed paleocave systems using GPR attributes. J. Appl. Geophys., **103**, 43–56, doi: 10.1016/j.jappgeo.2014.01.007.

El Hameedy M. A., Mabrouk W. M., Dahroug S., Youssef M. S., Metwally A. M., 2023a: Role of Seismic Refraction Tomography (SRT) in bedrock mapping; case study from industrial zone, Ain-Sokhna area, Egypt. Contrib. Geophys. Geod., **53**, 2, 111–128, doi: 10.31577/congeo.2023.53.2.2.

El Hameedy M. A., Mabrouk W. M., Dahroug S., Metwally A. M., 2023b: Detection of subsurface basaltic sheets and associated structures utilising forward modelling and inversion of 2D electrical resistivity data: A case study from Jebel-Qatrani, Fayoum, Egypt. Contrib. Geophys. Geod., **53**, 1, 43–63, doi: 10.31577/congeo.2023.53.1.3.

El-Qady G., Hafez M., Abdalla M. A., Ushijima K., 2005: Imaging subsurface cavities using geoelectric tomography and ground-penetrating radar. J. Cave Karst Stud., **67**, 174–181.

Encyclopædia Britannica: Cross-section of a cave. Image, https://www.britannica.com/science/karst-geology#/media/1/312718/112257, accessed 10 Nov. 2022.

Farag I. M., Ismail M. M., 1959: A contribution to the structure of the area east of Helwan. Egypt. J. Geol., **3**, 71–86.

Ganiyu S. A., Oladunjoye M. A., Onakoya O. I., Olutoki J. O., Badmus B. S., 2020: Combined electrical resistivity imaging and ground penetrating radar study for detection of buried utilities in Federal University of Agriculture, Abeokuta, Nigeria. Environ. Earth Sci., **79**, 177, doi: 10.1007/s12665-020-08919-2.

Gilli É., 2015: Karstology: karsts, caves and springs. Elements of fundamental and applied karstology. CRC Press, Boca Raton.

Gómez-Ortiz D., Martín-Crespo T., 2012: Assessing the risk of subsidence of a sinkhole collapse using ground penetrating radar and electrical resistivity tomography. Eng. Geol., **149–150**, 1–12, doi: 10.1016/j.enggeo.2012.07.022.

Grasmueck M., Quintà M. C., Pomar K., Eberli G. P., 2013: Diffraction imaging of subvertical fractures and karst with full-resolution 3D Ground-Penetrating Radar. Geophys. Prospect., **61**, 5, 907–918, doi: 10.1111/1365-2478.12004.

Günay G., Ekmeci M., Bayan C., Kurttas T., El-Bedewy F., 1997: A crescent shaped cave in Egypt. In: Günay G., Johnson A. (Eds.): Proceedings, symposium on karst waters and environmental imapacts. A. A. Balkema, Rotterdam, 257–263.

Hassan M. Y., Issawi B., Zaghloul E. A., 1978: Geology of the area east of Beni Suef, Eastern Desert, Egypt. Ann. Geol. Surv. Egypt, **8**, 129–162.

Issawi B., Ahmed S. M., Osman R., Sallam E. S., 2005: Studies on the Pliocene-Quaternary sediments in the western fringes of the Nile Delta-Lower Nile Valley stretch, Egypt. Sedimentology Egypt, **13**, 277–296.

Kruse S., Grasmueck M., Weiss M., Viggiano D., 2006: Sinkhole structure imaging in covered Karst terrain. Geophys. Res. Lett., **33**, 16, L16405, doi: 10.1029/2006GL026975.

Milanović P., Maksimovich N., Meshcheriakova O., 2019: Characterization of Surface and Underground Karst Features. In: Dams and Reservoirs in Evaporites. Advances in Karst Science. Springer, Cham, doi: 10.1007/978-3-030-18521-3_4.

Pueyo-Anchuela Ó., Casas-Sainz A. M., Soriano M. A., Pocoví-Juan A., 2010: A geophysical survey routine for the detection of doline areas in the surroundings of Zaragoza (NE Spain). Eng. Geol., **114**, 3-4, 382–396, doi: 10.1016/j.enggeo.2010.05.015.

Putiška R., Nikolaj M., Dostál I., Kušnirák, D., 2012: Determination of cavities using electrical resistivity tomography. Contrib. Geophys. Geod., **42**, 2, 201–211, doi: 10.2478/v10126-012-0018-3.

Redhaounia B., Aktarakçi H., Ilondo B. O., Gabtni H., Khomsi S., Bédir M., 2015: Hydrogeophysical interpretation of fractured and karstified limestones reservoirs: A case study from Amdoun region (NW Tunisia) using electrical resistivity tomography, digital elevation model (DEM) and hydro-geochemical approaches. J. Afr. Earth Sci., **112**, A, 328–338, doi: 10.1016/j.jafrearsci.2015.09.020.

Reynolds J. M., 2011: An Introduction to Applied and Environmental Geophysics. Preview, **2011**, 155, 33–40, doi: 10.1071/PVv2011n155other.

Sallam E., Wanas H. A., Osman R., 2015: Stratigraphy, facies analysis and sequence stratigraphy of the Eocene succession in the Shabrawet area (north Eastern Desert, Egypt): an example for a tectonically influenced inner ramp carbonate platform. Arab. J. Geosci., **8**, 12, 10433–10458, doi: 10.1007/s12517-015-1969-2.

Sallam E. S., Erdem N. Ö., Sinanoğlu D., Ruban D. A., 2018a: Mid-Eocene (Bartonian) larger benthic foraminifera from southeastern Turkey and northeastern Egypt: New evidence for the palaeobiogeography of the Tethyan carbonate platforms. J. Afr. Earth Sci., **141**, 70–85. doi: 10.1016/j.jafrearsci.2018.01.009.

Sallam E., Issawi B., Osman R., Ruban D., 2018b: Deposition in a changing paleogulf: evidence from the Pliocene–Quaternary sedimentary succession of the Nile Delta, Egypt. Arab. J. Geosci., **11**, 18, 558, doi: 10.1007/s12517-018-3919-2.

Sallam E. S., Ruban D. A., Mostafa M. T., Elkhodery M. Kh., Alwilily R. L., Molchanova T. K., Zorina S. O., 2020: Unique desert caves as a valuable geological resource: first detailed geological heritage assessment of the Sannur Cave, Egypt. Arab. J. Geosci., **13**, 141. doi: 10.1007/s12517-020-5176-4.

Sandmeier K. J., 2016: ReflexW Version 8.1. Program for Processing of Seismic, Acoustic or Electromagnetic Reflection, Refraction and Transmission Data. Software Manual, Karlsruhe, Germany, 628 p.

Slob E., Sato M., Olhoeft G., 2010: Surface and borehole ground-penetrating-radar developments. Geophysics, **75**, 5, 75A103–75A12, doi: 10.1190/1.3480619.

Stepišnik U., Trenchovska A., 2018: A New Quantitative Model for Comprehensive Geodiversity Evaluation: the Škocjan Caves Regional Park, Slovenia. Geoheritage,**10**, 1, 39–48 (2018). doi: 10.1007/s12371-017-0216-5.

Telford W. M., Geldart L. P., Sheriff R. E., 1990: Applied geophysics. 2nd Ed., Cambridge University Press, Cambridge, 770 p.

Tomassetti M. C., Lucarini G., Hamdan M. A., Macchia A., Mutri G., Barich B. E., 2016: Preservation and restoration of the Wadi Sura caves in the framework of the "Gilf Kebir National Park", Egypt. Int. J. Conserv. Sci., **7**, spec. issue 2, 913–934.

Vermeersch P. M., Van Peer P., Rots V., Paulussen R., 2005: A survey of the Bili Cave and its surroundings in the Red Sea Mountains, El Gouna, Egypt. J. Afr. Archaeol., **3**, 2, 267–276, doi: 10.3213/1612-1651-10054.

Spichak V. V., 2020: Electromagnetic study of geothermal areas. In: Spichak V. V. (Ed.): Computational Geophysics, Computational Geo-Electromagnetics. Elsevier **5**, 167–205, doi: 10.1016/B978-0-12-819631-1.00006-7.

Wanas H. A., Pickford M., Mein P., Soliman H., Segalen L., 2009: Late Miocene karst system at Sheikh Abdallah, between Bahariya and Farafra, Western Desert, Egypt: Implications for palaeoclimate and geomorphology. Geol. Acta **7**, 4, 475–487, doi: 10.1344/105.000001450.

Xavier Neto P., de Medeiros W. E., 2006: A practical approach to correct attenuation effects in GPR data. J. Appl. Geophys., **59**, 2, 140–151, doi: 10.1016/j.jappgeo.2005.09.002.

Xie P., Wen H., Xiao P., Zhang Y., 2018: Evaluation of ground-penetrating radar (GPR) and geology survey for slope stability study in mantled karst region. Environ. Earth Sci., **77**, 122, doi: 10.1007/s12665-018-7306-9.

Zhou B., 2018: Electrical Resistivity Tomography: A Subsurface-Imaging Technique. In: KanlıA. I. (Ed.): Applied Geophysics with Case Studies on Environmental, Exploration and Engineering Geophysics. IntechOpen, doi: 10.5772/intechopen.81511.

Zhou W., Beck B. F., Adams A. L., 2002: Effective electrode array in mapping karst hazards in electrical resistivity tomography. Environ. Geol., **42**, 8, 922–928, doi: 10.1007/s00254-002-0594-z.